Extreme multiplicity in cylindrical Rayleigh-Bénard convection. I. Time dependence and oscillations

Katarzyna Borońska* and Laurette S. Tuckerman†
Laboratoire d'Informatique pour la Mécanique et les Sciences de l'Ingénieur (LIMSI-CNRS), BP 133, 91403 Orsay, France
(Received 29 August 2009; published 26 March 2010)

Rayleigh-Bénard convection in a cylindrical container can take on many different spatial forms. Motivated by the results of Hof *et al.* [Phys. Fluids **11**, 2815 (1999)], who observed coexistence of several stable states at a single set of parameter values, we have carried out simulations at the same Prandtl number, that of water, and a radius-to-height aspect ratio of two. We have used two kinds of thermal boundary conditions: perfectly insulating sidewalls and perfectly conducting sidewalls. In both cases we obtain a wide variety of coexisting steady and time-dependent flows.

DOI: 10.1103/PhysRevE.81.036320 PACS number(s): 47.20.Ky, 47.20.Bp, 47.10.Fg, 47.11.Kb

I. INTRODUCTION

The flow patterns realized by Rayleigh-Bénard convection depend not only on the fluid parameters and container geometry, but also on the flow history. This was strikingly illustrated by the experimental study carried out by Hof *et al.* [1,2]. They investigated a cylinder of small aspect ratio $\Gamma \equiv \text{radius}/\text{height}=2.0$ filled with water (Prandtl number of 6.7). Varying the Rayleigh number through different sequences of values, they obtained several different stable patterns for the same final Rayleigh number. For 14 200 they observed two, three, and four parallel rolls, a "Mercedes" pattern with three spokes of ascending or descending fluid and even an axisymmetric state (Fig. 1). They also reported a transition from an axisymmetric steady state toward azimuthal waves.

We begin by reviewing the literature on Rayleigh-Bénard convection in cylinders with small-to-moderate aspect ratios $1 \lesssim \Gamma \lesssim 10$. Our interest in such geometries stems from the fact that they are the battleground of two competing tendencies over an appreciable Rayleigh-number range. At threshold, the patterns necessarily resemble eigenmodes of the Laplacian, i.e., they are trigonometric in the azimuthal angle. But at higher Ra, the patterns form rolls, bending and pinching so as to fit into the cylinder.

The instability of the conductive state in a cylindrical geometry was well established in the 1970s–1980s [3–6]. Critical Rayleigh numbers Ra_c are about 2000 for $\Gamma \sim 1$, increasing steeply for lower Γ and decreasing asymptotically toward $\mathrm{Ra}_c=1708$ for $\Gamma \to \infty$. The seminal paper of Buell and Catton [6] surveyed the influence of sidewall conductivity on the onset of convection by performing linear analysis for the aspect ratio range $0<\Gamma \leq 4$. They determined the critical Rayleigh number and the azimuthal wave number as a function of both aspect ratio and sidewall conductivity, thus completing the results of the previous investigations, which considered either perfectly insulating or perfectly conducting walls. The flow succeeding the conductive state is three-dimensional over large ranges of aspect ratios, contrary to the expectations of Koschmieder [7]. Similar calculations were carried out by Marques *et al.* [8].

The stability of the first convective state, for situations in which the primary flow is axisymmetric, was investigated in the 1980s–1990s [9–12] for a variety of aspect ratios and Prandtl numbers. Bifurcation-theoretic scenarios for axisymmetric flows have been investigated by Barkley and Tuckerman [13] and Siggers [14]. Experiments on the competition between various convective patterns in a constrained cylindrical geometry ($\Gamma \approx 7.5$) were carried out during this period [15–17] and the dynamics were interpreted in terms of the instabilities of two-dimensional straight rolls [18].

Several time-dependent simulations since 2000 focused on the variety of coexisting nonaxisymmetric patterns for $\Gamma \approx 4$. Rüdiger and Feudel [19] used a spectral simulation to investigate the aspect ratio $\Gamma=4$, finding the stability ranges of several patterns—parallel rolls, target, and spirals—with overlapping stability ranges in Rayleigh number. Paul *et al.* [20] studied the dislocation dynamics of curved rolls near the onset.

Several studies have focused on configurations similar or identical to that of Hof *et al.* [1]. Leong [21] used a finite

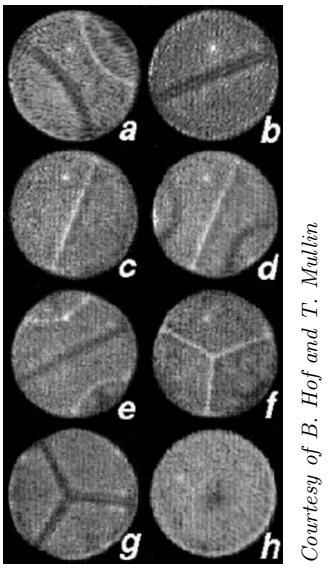

FIG. 1. Patterns observed in the experiment of Hof *et al.* at $\mathrm{Ra}=14\,200$. (a) three rolls, (b) two rolls, (c) inverted two rolls, (d) four rolls, (e) inverted four rolls, (f) Mercedes, (g) inverted Mercedes, and (h) axisymmetric pattern. Dark areas correspond to hot (rising) and bright to cold (descending) fluid.

*www.comp.leeds.ac.uk/kb; k.boronska@leeds.ac.uk
†www.pmmh.espci.fr/~laurette; laurette@pmmh.espci.fr

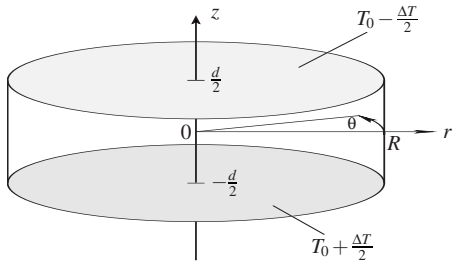

FIG. 2. Geometry and coordinate system.

difference method to simulate convective flows for Prandtl number Pr=7 in cylinders of aspect ratios $\Gamma=2$ and 4 and adiabatic lateral walls. He observed several steady patterns—parallel rolls, three-spoke flow and axisymmetric state—all of which were stable in the range $6250 \leq \mathrm{Ra} \leq 37\,500$. Ma *et al.* [22] used a finite volume method to simulate the parameters $\Gamma=2$ and Pr=6.7 of Hof *et al.* [1]. As in our prior study [23], they used time-dependent simulation at Ra=14 200 to reproduce the five states of Hof *et al.* They also calculated the first nine primary bifurcations to modes of varying azimuthal wave numbers and several secondary bifurcations, all taking place for $\mathrm{Ra} \leq 2500$. However, they reported no results for Ra between 2500 and 14 200, or for any values above 14 200.

The work we present here is based on that of Borońska [23] and covers simulations of $\Gamma=2$ and Pr=6.7 over the entire Rayleigh-number range up to 30 000. We carry out a complete survey of the convective patterns we locate; we then carry out the same study for the case of conductive sidewalls. A companion paper [24] takes the present paper as a starting point to compute a bifurcation diagram for the insulating sidewall case over the range $\mathrm{Ra} \leq 30\,000$, which connects the patterns at Ra=14 200 with the primary bifurcations from the conductive branch.

II. GOVERNING EQUATIONS AND NUMERICAL METHODS

The methods used in our study are described in this section. We first present the nonlinear equations governing the system. We then describe the most important aspects of the numerical methods used for integrating the differential equations. A detailed description of all numerical techniques used can be found in [25].

A. Equations and boundary conditions

We consider a fluid confined in a cylinder of depth d and radius R, whose aspect ratio is defined as $\Gamma \equiv R/d$ (Fig. 2). The fluid has kinematic viscosity ν, density ρ, thermal diffusivity κ, and thermal expansion coefficient (at constant pressure) γ. The top and bottom temperatures of the cylinder are kept constant, at $T_0-\Delta T/2$ and $T_0+\Delta T/2$, respectively. The Rayleigh number Ra and the Prandtl number Pr are defined by

$$\mathrm{Ra} \equiv \frac{\Delta T g \gamma d^3}{\kappa \nu}, \quad \mathrm{Pr} \equiv \frac{\nu}{\kappa}. \tag{1}$$

Using the units d^2/κ, d, κ/d, and $\nu\kappa/\gamma g d^3$ for time, distance, velocity, and temperature, and defining H to be the dimensionless temperature deviation from the linear vertical profile, we obtain the Navier-Stokes and Boussinesq dimensionless equations governing the system,

$$\partial_t H + (\mathbf{U}\cdot\nabla)H = \mathrm{Ra}\, U_z + \nabla^2 H, \tag{2a}$$

$$\mathrm{Pr}^{-1}[\partial_t \mathbf{U} + (\mathbf{U}\cdot\nabla)\mathbf{U}] = -\nabla P + \nabla^2 \mathbf{U} + H\mathbf{e}_z, \tag{2b}$$

$$\nabla\cdot\mathbf{U} = 0. \tag{2c}$$

We used realistic boundary conditions for the velocity, with no-penetration and no-slip on the horizontal plates and sidewalls,

$$\mathbf{U} = 0 \quad \text{for } z = \pm 1/2 \quad \text{or } r = \Gamma. \tag{3a}$$

We assume that perfectly conducting horizontal plates maintain the temperature constant (homogeneous Dirichlet condition for H),

$$H = 0 \quad \text{for } z = \pm 1/2. \tag{3b}$$

The sidewalls are either perfectly insulating (Neumann boundary conditions),

$$\partial_r H = 0 \quad \text{for } r = \Gamma, \tag{3c}$$

or perfectly conducting, so that a linear vertical temperature profile is maintained within them (Dirichlet boundary conditions),

$$H = 0 \quad \text{for } r = \Gamma. \tag{3d}$$

The code has also a possibility that we have not utilized here of interpolating between these two conditions in order to represent sidewalls with finite values of conductivity, as was done in [13],

$$\mu_{Dir} H + \mu_{Neu}\partial_r H = 0 \quad \text{for } r = \Gamma. \tag{4}$$

B. Spatial and temporal discretization

We represent the fields by a tensor product of trigonometric functions in θ and Chebyshev polynomials on the intervals $-1/2 \leq z \leq 1/2$ and $0 \leq r \leq \Gamma$. A representation which is regular at the origin can be created by imposing parity restrictions on the Chebyshev and Fourier functions [25]. The temperature and vertical velocity are approximated by the formula

$$f(r,\theta,z) = \sum_{m=0}^{N_\theta/2} \sum_{\substack{j\geq m \\ j+m \text{ even}}}^{2N_r-1} \sum_{k=0}^{N_z-1} \hat{f}_{j,m,k} T_j(r/\Gamma) T_k(2z) e^{im\theta} + \text{c.c.} \tag{5}$$

For the radial and azimuthal velocity components, the same representation is used, except with $j+m$ odd. In the code, less stringent parity rules are used, ensuring only that the first three derivatives of f are continuous at the cylinder axis. The pseudospectral method [26] calls for carrying out differentiation on the spectral representation on the right-hand side of Eq. (5). Multiplication is carried out by first transforming to a representation on a Gauss-Lobatto grid, which includes the

boundary points. The Fourier transforms, including cosine transforms for the Chebyshev polynomials, use the Temperton algorithms [27] for dimensions which are not restricted to powers of 2. Radial and axial boundary conditions are imposed via the tau method, i.e., replacing the equations corresponding to the highest-order Chebyshev polynomials with the boundary conditions.

The temporal discretization is semi-implicit. The viscous, diffusive, and buoyancy terms are integrated via the backward Euler scheme while the advective terms are integrated via the Adams-Bashforth scheme. Applying these formulas to Eqs. (2a) and (2b), we obtain

$$(1-\Delta t\nabla^2)H^{n+1} = H^n + \frac{\Delta t}{2}[-3(\mathbf{U}^n\cdot\nabla)H^n + (\mathbf{U}^{n-1}\cdot\nabla)H^{n-1} + \mathrm{Ra}(3U_z^n - U_z^{n-1})], \tag{6a}$$

$$(1-\Delta t\ \mathrm{Pr}\ \nabla^2)\mathbf{U}^{n+1} + \Delta t\ \mathrm{Pr}\ \nabla P^{n+1} = \mathbf{U}^n + \frac{\Delta t}{2}[-3(\mathbf{U}^n\cdot\nabla)\mathbf{U}^n + (\mathbf{U}^{n-1}\cdot\nabla)\mathbf{U}^{n-1}] + \Delta t\ \mathrm{Pr}\ H^{n+1}\mathbf{e}_z. \tag{6b}$$

In the Helmholtz operators on the left-hand sides of Eqs. (6), each Fourier mode m in representation (5) is decoupled from the other Fourier modes. In addition to this economy, for each m, the matrix representing a differential operator can be diagonalized in the z direction [28] and reduced to a banded matrix in the r direction [29]. The storage and the time for inversion of the resulting linear systems are then on the order of $N_\theta N_r N_z^2$.

C. Resolution

In order to choose our spatial resolution, we carried out several runs at varying resolution at a Rayleigh number of 14 000 and time step $\Delta t = 2\times 10^{-4}$, comparing the evolution of several quantities, such as temperature and velocity at fixed grid points, several spectral coefficients, and the total energy

$$E \equiv \frac{1}{\mathrm{Ra}}\left(\frac{1}{\mathrm{Pr}}\int_{\mathrm{vol}}\mathbf{U}\cdot\mathbf{U} + \frac{1}{\mathrm{Ra}}\int_{\mathrm{vol}}H^2\right). \tag{7}$$

The resolution $N_r\times N_\theta\times N_z = 40\times 120\times 20$ was chosen as a compromise between accuracy and efficiency. This resolution insured that the spectral coefficients decayed exponentially with wave number or Chebyshev index. We also reproduced a few high Rayleigh-number states ($20\,000 \le \mathrm{Ra} \le 30\,000$) at the higher resolution $N_r\times N_\theta\times N_z = 60\times 160\times 30$. In the case of any uncertainty concerning the resulting pattern, the mesh was refined; each such test confirmed the results obtained with the previous resolution.

The time step Δt chosen depends on the Rayleigh number and on the evolution of the system. For higher Rayleigh numbers and abrupt transitions, a smaller time step is required. For slowly evolving fields, the number of iterations necessary for convergence becomes too great, unless we use larger Δt. We chose the initial time steps as a function of Rayleigh number and, if the evolution slowed down, we continued the simulation with an increased Δt. The time steps we used varied from $\Delta t = 8\times 10^{-4}$ for Ra=2000 to $\Delta t = 2\times 10^{-4}$ for Ra=30 000. The time step was reduced when necessary, especially when any oscillations appeared.

D. Incompressibility: Velocity-pressure decoupling

In order to decouple velocity and pressure, the divergence operator is applied to Eq. (6b) to derive a Poisson equation for P,

$$\nabla^2 P = \nabla\cdot\left(\frac{1}{2\ \mathrm{Pr}}[-3(\mathbf{U}^n\cdot\nabla)\mathbf{U}^n + (\mathbf{U}^{n-1}\cdot\nabla)\mathbf{U}^{n-1}] + H^{n+1}\mathbf{e}_z\right), \tag{8}$$

where $\nabla\cdot U^n = \nabla\cdot U^{n+1} = 0$ and $\nabla\cdot\nabla^2 = \nabla^2\nabla\cdot$ have been used. The thorny issue of boundary conditions for this Poisson equation can be addressed in several ways [25,30]. Most approaches derive boundary conditions for P from the original momentum equation (2b). This will yield a divergence which is proportional to a power of Δt. This is usually acceptable for time integration, where Δt is small. However, to carry out Newton's method for steady-state solving, as we will do in our companion paper [24], we adapt this time-stepping code, using $\Delta t \gg 1$. We therefore require a method that imposes incompressibility regardless of Δt. Essentially, the correct boundary condition for Eq. (8) is

$$\nabla\cdot\mathbf{U} = 0 \quad \text{for } z = \pm 1/2 \quad \text{or } r = \Gamma, \tag{9}$$

which again couples velocity and pressure.

We use a Green's function or influence matrix method [25] as follows. In a preprocessing step, we calculate a set of *homogeneous* solutions $\mathbf{U}^{\mathrm{hom},j}$:

(h,i) We solve the homogeneous version of the pressure Poisson equation (8) with all possible Dirichlet boundary conditions for P, for example, by choosing each point $\mathbf{x}_j$ on the boundary in turn and setting the boundary conditions to be 1 at $\mathbf{x}_j$ and 0 elsewhere. (An equivalent approach would loop over all of the highest Chebyshev components.) This yields a set of homogeneous pressure solutions $P^{\mathrm{hom},j}$.

(h,ii) We then solve the homogeneous version of Eq. (6b), i.e., setting the right-hand side to zero, setting $P = P^{\mathrm{hom},j}$, and imposing the homogeneous boundary conditions (3). This yields a set of homogeneous velocity solutions $\mathbf{U}^{\mathrm{hom},j}$.

(h,iii) We complete the preprocessing step by calculating $\mathcal{C}_{ij} \equiv \nabla\cdot\mathbf{U}^{\mathrm{hom},j}(\mathbf{x}_i)$ on all points $\mathbf{x}_i$ of the boundary. $\mathcal{C}$ is the influence (or capacitance) matrix.

At each time step, we calculate a *particular* solution $\mathbf{U}^{\mathrm{part}}$ and then the final solution $\mathbf{U}$ as follows:

(p,i) We solve the pressure Poisson equation (8) with the nonzero right-hand side in Eq. (8), but with homogeneous Dirichlet boundary conditions for P. This yields the particular pressure P^{part}.

(p,ii) We solve Eq. (6b) for the velocity, using $P = P^{\mathrm{part}}$ and imposing the homogeneous boundary conditions (3a). This yields the particular velocity $\mathbf{U}^{\mathrm{part}}$.

(p,iii) We calculate $\nabla\cdot\mathbf{U}^{\mathrm{part}}(\mathbf{x}_i)$, the divergence of the particular velocity on each point on the boundary.

(p,iv) By solving the linear system

$$0 = \nabla \cdot \mathbf{U}^{\text{part}}(\mathbf{x}_i) + \sum_j c_j \nabla \cdot \mathbf{U}^{\text{hom},j}(\mathbf{x}_i), \tag{10}$$

involving the influence matrix, we determine the coefficients c_j.

(p,v) The final solution is assembled as

$$\mathbf{U}^{n+1} = \mathbf{U}^{\text{part}} + \sum_j c_j \mathbf{U}^{\text{hom},j}. \tag{11}$$

Alternatively, if the homogeneous solutions $\mathbf{U}^{\text{hom},j}$ are not stored, we obtain the final solution by repeating steps (p,i) and (p,ii), but using the coefficients c_j as inhomogeneous Dirichlet boundary conditions for P.

We point out several final aspects of this influence matrix method:

(i) As mentioned previously, the differential operators are decoupled by azimuthal Fourier mode; this also applies to the influence matrix, making its size manageable, i.e., $(2N_r+N_z)\times(2N_r+N_z)$ for each m.

(ii) Because system (10) is in fact overdetermined, the influence matrix must be regularized (e.g., zero eigenvalues replaced with finite values) in order to be inverted.

(iii) Although $\nabla\cdot$ and ∇^2 commute, even for the discretized operators, this is no longer the case when boundary conditions are substituted for the highest-order equations, essentially because differentiation lowers the polynomial order. The *tau correction* keeps track of the derivatives of the dropped frequencies; and, once the solution is obtained, the necessary correction is applied to it. In the code, the tau correction is implemented in the influence matrix, along with the boundary conditions.

E. Computing details

We used a simulation code written in FORTRAN in the 1980s [25], slightly modernized and optimized for vector platforms NEC SX-5 and NEC SX-8. The Fourier transforms used to convert from the spectral to the physical representation (in which the nonlinear term is computed at each time step) were carried out by the NEC emulation of the SciLib Cray library. A typical three-dimensional nonlinear run of 1000 time steps required 70 CPU seconds. Patterns were visualized using the VTK library. The color map we used is based on CMRMAP [31], in which luminosity changes monotonically. Thus, visualizations are correctly rendered in gray scale as well as in color.

III. RESULTS

A. Insulating sidewalls

We have performed a sequence of simulations, varying the initial state and the Rayleigh number, in order to find the asymptotic state for each configuration. We chose to use Neumann boundary conditions for the temperature deviation on the sidewalls, which corresponds to perfect insulation. This should be close to the experimental setup, where Perspex Plexiglas (a poor thermal conductor) was used.

1. Experimental and numerical protocol

In their experiment, Hof *et al.* [1] produced the large number of convective patterns at Ra=14 200 shown in Fig. 1 by increasing and decreasing the Rayleigh number in a variety of ways. The three-roll state in Fig. 1(a) was obtained by starting from a subcritical Rayleigh number and gradually increasing Ra in steps of ΔRa=200. A further increase in Ra to 21 200 followed by a decrease in 14 200 led to the two-roll state in Fig. 1(b). The four-roll state [Fig. 1(d)] was obtained by a sudden increase in Ra from a subcritical value to 13 000 followed by a slow increase to 14 200, while the axisymmetric state [Fig. 1(h)] was obtained by a sudden increase to 15 000 followed by a slow decrease. The inverted [Figs. 1(c) and 1(e)] and Mercedes [Figs. 1(f) and 1(g)] patterns, as well as rotating and pulsating patterns not shown in Fig. 1, were obtained by more complicated sequences.

Rather than filling in the entire set of combinations of Rayleigh numbers and initial conditions, we attempted to probe this parameter space. We initialized the simulations with a slightly perturbed conductive solution. This can be seen as corresponding to a sudden jump of heating power in an experimental setup, where previously a fluid was maintained below the convection threshold. Such simulations gave us different patterns, depending on Rayleigh number. Once we obtained these stable convective flows, we used them as initial states at other Rayleigh numbers. This is again comparable to an experimental situation in which, once a pattern is stabilized, the heating power is changed abruptly.

In order to qualify a solution as stable, we monitored the evolution of the flow structure, its energy, and the azimuthal velocity at two arbitrarily chosen points. We qualified a state as stable if the observed quantities did not change more than about 0.1% over 2–4 diffusive time units and seemed to saturate. We were especially careful about classifying as stable a state we qualified already as transitional for another Rayleigh number. We cannot, however, exclude the possibility that a long-lasting transitional state was interpreted as stable; see our companion paper [24].

The field visualized throughout this paper is the temperature deviation from the basic vertical profile, referred to merely as the temperature, as for fixed z they differ only by a constant. The horizontal cuts are taken in the midplane; dark (bright) areas indicate hot (cold) zones. The time is expressed in dimensionless units of the vertical thermal diffusion time $[t]=d^2/\kappa$.

The patterns we observed and the transitions between them are described in the sections that follow. In order to orient the reader, we anticipate these results and present in Fig. 3 a schematic diagram of the stable patterns we observed for different Rayleigh numbers. More quantitative diagrams can be found at the end of Sec. III A.

2. Sudden start from a perturbed conductive state

We first report the results obtained from the slightly perturbed conductive solution, shown in Fig. 3(a). We run a series of simulations for Rayleigh numbers between 1600

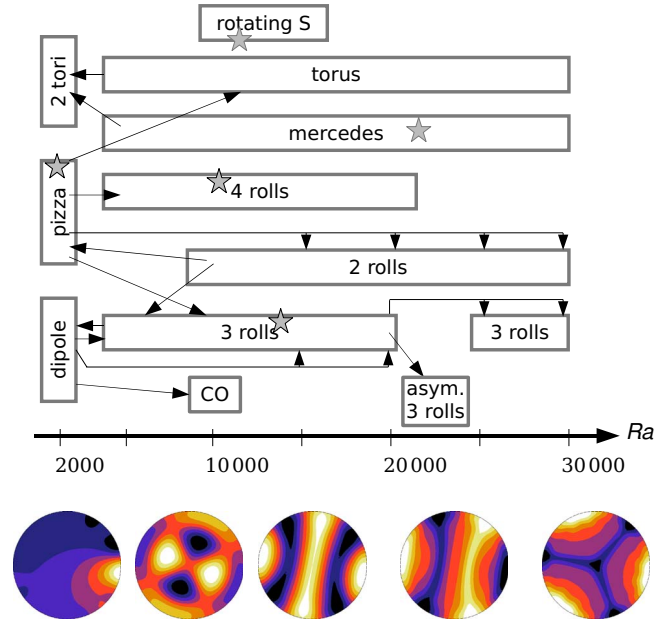

(a) initial perturbation (b) pizza, Ra = 2400 (c) four rolls, Ra = 5000 (d) three rolls, Ra = 12 000 (e) mercedes, Ra = 23 000

FIG. 3. (Color online) Schematic diagram of stability ranges and transitions between convective patterns as a function of Rayleigh number for $\Gamma=2$, Pr=6.7 and insulating sidewalls. Stars denote solutions obtained from a sudden start to the Rayleigh number indicated, using as an initial condition a slightly perturbed conductive state. (a) Initial perturbation. (b)–(e) Convective patterns obtained from a sudden start to Rayleigh numbers indicated. Visualization of the temperature in the cylinder's midplane, dark, hot (ascending), bright, cold (descending) fluid.

and 23 000. Depending on the Rayleigh number, this state evolves toward different flows shown in Figs. 3(b)–3(e).

For Ra$\lesssim$1900, the initial perturbation decays to zero, i.e., the conductive state. For Ra near 2000, the final state is a quadrupole pattern which we will call the *pizza state* [shown in Fig. 3(b)]. This state has four well-separated sections, resembling pieces of a pizza. Each section has either a hot round spot in the center with a colder area along the sidewall or a cold round spot in the center with a warmer area at the sidewall.

For Ra between approximately 3000 and 20 000, the system evolves toward states with parallel or rather quasiparallel rolls. Between 3000 and 10 000 the final state has four rolls, as in the example depicted in Fig. 3(c), which has up-flow (light areas) along the central diameter and two small regions on the left and right boundaries, with down-flow (dark areas) in between. Between 10 000 and 20 000, the final solution has three rolls; that in Fig. 3(d) has up-flow to the right and down-flow to the left of the central diameter, delimiting a wide central roll, with a smaller roll on either side. Finally, for Ra$\approx$23 000, the final pattern consists of three radial spokes of cold descending fluid [Fig. 3(e)], named the *Mercedes* pattern by Hof [2]. For all these patterns, the roll boundaries become thinner as the Rayleigh number is increased.

In Hof's experiments, a sudden increase to Ra=13 000 and 15 000 led to a four-roll and an axisymmetric pattern,

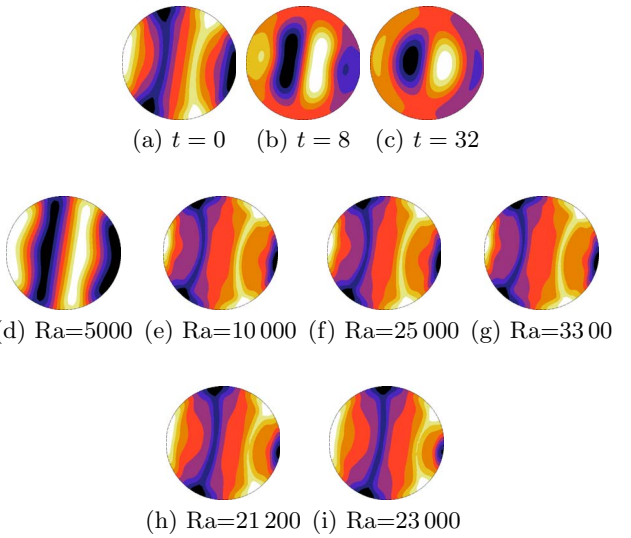

(a) $t=0$ (b) $t=8$ (c) $t=32$

(d) Ra=5000 (e) Ra=10 000 (f) Ra=25 000 (g) Ra=33 00

(h) Ra=21 200 (i) Ra=23 000

FIG. 4. (Color online) Evolution from three-roll pattern. (a)–(c) Evolution at Ra=2000 leading towards dipole. (d)–(g) Three-roll patterns at different Rayleigh numbers. (h)–(i) Asymmetric three-roll pattern with central roll shifted to the right, obtained for Ra between 20 000 and 25 000.

respectively. However, Fig. 3, which summarizes the results of all of our simulations, shows that we were able to produce four-roll and axisymmetric patterns at these Rayleigh numbers by other routes.

3. Three-roll patterns

In the second series of simulations, we used as the initial condition the three-roll state previously converged at Ra =14 200, like that in Fig. 3(d). Below the critical Rayleigh number this pattern decays to zero via an intermediate *dipole pattern* and for Ra=2000 the three rolls transform into a dipole state, as shown in Figs. 4(a)–4(c).

For Ra=5000 and above, up to Ra=33 000, the three-roll state remains stable, with the rolls more curved for higher Rayleigh numbers, as shown in Figs. 4(d)–4(g). An exception is the range between Ra=20 000 and 25 000, where this pattern becomes asymmetric—the band of colder fluid between the central roll and the left roll moves slightly toward the center as the Rayleigh number is increased, as shown in Figs. 4(h) and 4(i). This is similar to the results of Hof *et al.* [1], although they found that the leftmost roll vanishes eventually at Ra=21 000, where the flow forms a two-roll pattern.

Figure 5 shows the Rayleigh-number dependence of the temperature at a fixed point and of the energy; both show deviations in the range 20 000$<$Ra$<$25 000. We conclude that a bifurcation is present. In the experiment this evolution yielded a two-roll pattern and, during our further analysis of two-roll states, we found that their energy indeed approaches that of shifted (asymmetric) three rolls.

4. Evolution from four rolls

We used a four-roll pattern converged at Ra=3000, like that in Fig. 3(c), as an initial condition for simulations at

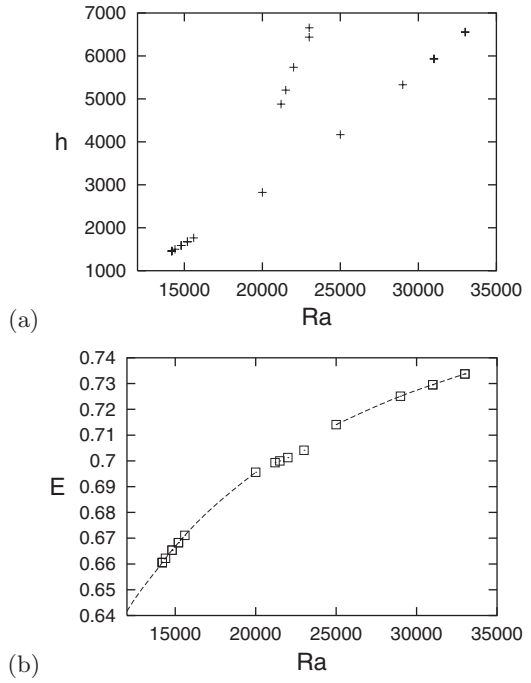

FIG. 5. Dependence of the three-roll patterns on Rayleigh number: (a) temperature at r=0.3, z=0.25, and θ=0; (b) energy.

$4000 \leq \mathrm{Ra} \leq 20\,000$. The newly evolved patterns are also of the four-roll family, and, as in the case of three rolls, the roll boundaries become thinner as the Rayleigh number is increased, as shown in Figs. 6(a)–6(c). We then used the four-roll state converged for Ra=20 000 depicted in Fig. 6(c) as an initial condition at Rayleigh numbers of 25 000 and 29 000. This time the geometry of the pattern changes, as displayed in Figs. 6(d)–6(h)—the four-roll pattern turns into a *cross pattern* with four spokes of descending cold fluid. The cross flow did not saturate in the time during which we observed it, but continued to evolve slowly; we suspect that it is a transitional rather than an asymptotic state. This would be in agreement with Hof [32], who observed that the cross pattern is a long-lasting transient state unstable to a Mercedes pattern.

5. Evolution from pizza pattern

We used the pizza pattern at Ra=2000, like that in Fig. 3(b), as an initial condition for a series of simulations

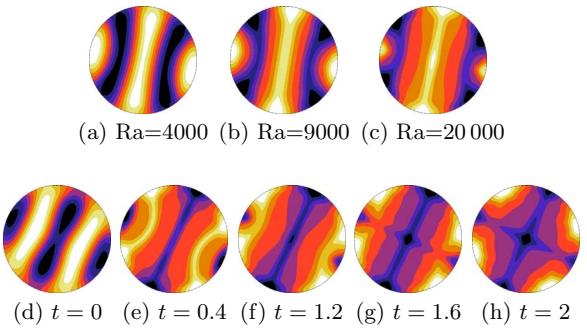

FIG. 6. (Color online) (a)–(c) Four-roll patterns for different Rayleigh numbers. (d)–(h) Evolution of the four-roll pattern towards (probably transitional) cross pattern at Ra=25 000

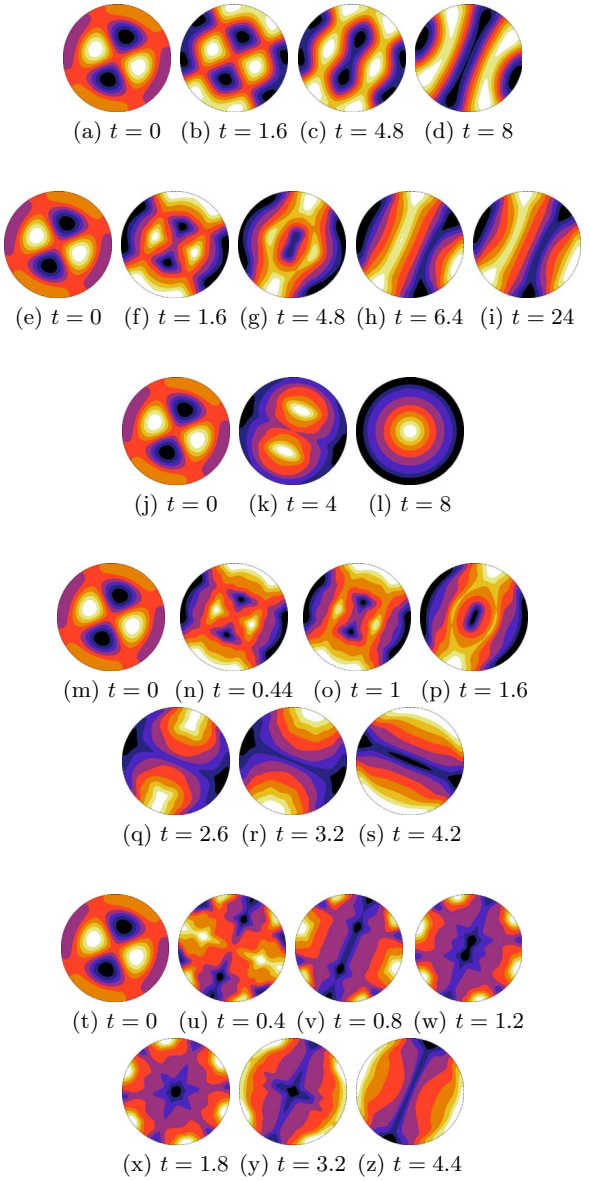

FIG. 7. (Color online) Evolution from pizza pattern. (a)–(d) To four-roll pattern at Ra=5000. (e)–(i) To three-roll pattern at Ra=10 000. (j)–(l) Through eight to final torus pattern at Ra=14 200. (m)–(s) Through a series of intermediate states towards final two-roll pattern at Ra=16 000. (t)–(z) Through a series of intermediate states towards final two-roll pattern at Ra=29 000.

at several Rayleigh numbers between 5000 and 29 000. In this range the pizza pattern is not stable. For Ra=5000 it changes into four rolls, as shown in Figs. 7(a)–7(d)) and for Ra=10 000 into three rolls, as in Figs. 7(e)–7(i). For Ra=14 200 the initial pizza flow evolves into a *torus pattern*—an axisymmetric state with one toroidal roll, passing through an intermediate *eight-pattern*. This evolution is displayed in Figs. 7(j)–7(l). The transitional eight-pattern was also observed by Hof [32].

For $\mathrm{Ra} \geq 15\,000$ the pizza state, after passing through a series of various transitional patterns, eventually evolves to a two-roll flow. Figures 7(m)–7(s) display the evolution of the system for Ra=16 000, where we describe the intermediate

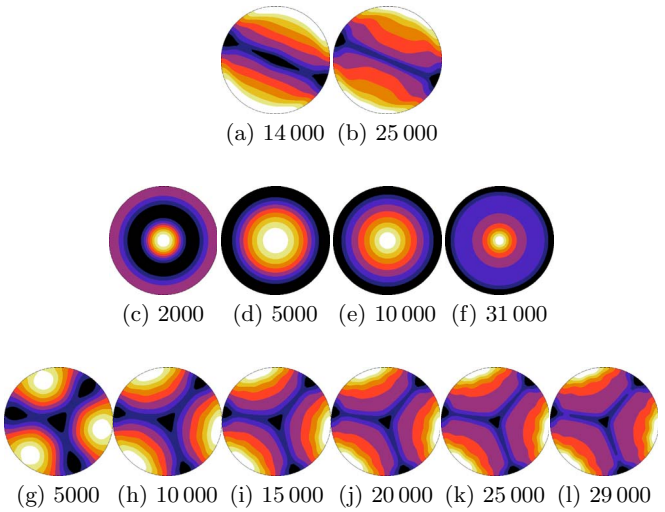

FIG. 8. (Color online) (a)–(b) Two-roll patterns. (c)–(f) Axisymmetric patterns. (g)–(l) Mercedes patterns. Rayleigh numbers as indicated below each visualization.

states as *triangle mosaic* [Fig. 7(n)], *eye* [Fig. 7(p)], and *imperfect eight* [Fig. 7(r)]. Figures 7(t)–7(z) present the system behavior for Ra=29 000, where the intermediate patterns between pizza and two rolls are *six-spoke elongated star* [Fig. 7(w)] and *six-spoke star* [Fig. 7(x)].

6. Evolution from two rolls

Another initial condition we used was the two-roll state like that in Fig. 7(s), converged previously at Ra=15 000. For Ra=2000 it leads to the pizza pattern, and for Ra =5000 to a three-roll state. For $10\,000 \leq \mathrm{Ra} < 29\,000$, we found the two-roll pattern to be stable. At Ra=29 000 the roll boundaries start oscillating slightly. Figures 8(a) and 8(b) present two-roll flow visualizations for different Rayleigh numbers.

7. Axisymmetric flows

The axisymmetric pattern, shown in Fig. 7(l) and used as an initial condition, also leads to axisymmetric patterns for a wide range of Rayleigh numbers $2000 \leq \mathrm{Ra} \leq 33\,000$, shown in Figs. 8(c)–8(f). For Ra=2000 there are two concentric toroidal rolls instead of one. This is in partial agreement with Hof [2], who found toroidal flow to be stable for Ra>3500, but to evolve toward a rotating three-petal pattern for $\mathrm{Ra} \gtrsim 23\,000$. At these values of Ra, our simulations still converge toward a stationary axisymmetric flow, although in an oscillatory manner. All axisymmetric patterns we observed were truly two dimensional, with no azimuthal velocity.

8. Evolution from Mercedes pattern

We ran a series of simulations using as the initial condition the Mercedes pattern in Fig. 3(e). For every Rayleigh number in the range $5000 \leq \mathrm{Ra} \leq 29\,000$ this gave stable Mercedes patterns and for Ra=2000 it evolves to a two-roll axisymmetric pattern. Figures 8(g)–8(l) display the final patterns for different Rayleigh numbers.

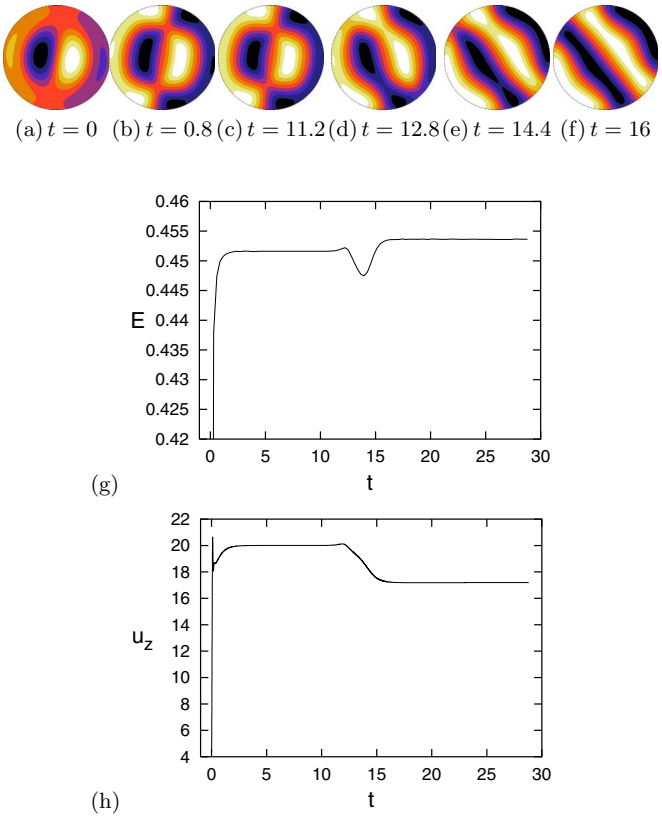

FIG. 9. (Color online) Evolution from dipole pattern to three-roll pattern at Ra=5000. (a)–(f) Visualizations at time indicated. Evolution as a function of time of (g) energy and (h) vertical velocity at one point. A long-lasting transient state is visible between $t=3$ and $t=12$

9. Evolution from dipole pattern

Another initial condition we used was the dipole pattern shown in Fig. 4(c). For Rayleigh numbers between 5000 and 29 000, with the exception of 10 000, the flow evolves toward a three-roll pattern. The evolution of the flow at Ra =5000 is presented in Fig. 9. At this Rayleigh number the system passes through a long-lasting intermediate *dipole smile state*, shown in Fig. 9(c), whose lifetime is of order 10. The flow patterns appearing for Ra=10 000 are depicted in Figs. 10(a)–10(c). An intermediate dipole smile state appears in Fig. 10(b), with a lifetime of about 2. The final solution is a *CO pattern*, shown in Fig. 10(c), composed of one curved and one circular roll. This state resembles the three-roll pattern with the ends of two neighboring rolls joined together, but its energy is higher than that of the three-roll state at the same Ra. At higher Rayleigh numbers, where the asymptotic solution is again a three-roll flow, transitional patterns also appear, shown in Figs. 10(d) and 10(e). The final patterns are shown in Figs. 10(g)–10(j), with the initial dipole pattern for comparison. The initial pattern orientation does not seem to determine the direction of the rolls of the final pattern. Figure 11 depicts the energy of patterns evolved starting from a dipole pattern as a function of Rayleigh number. For comparison, the energy of three-roll states from Sec. III A 3 is also displayed. They are in perfect agreement with the sole exception of Ra=10 000: the energy of the CO state is lower.

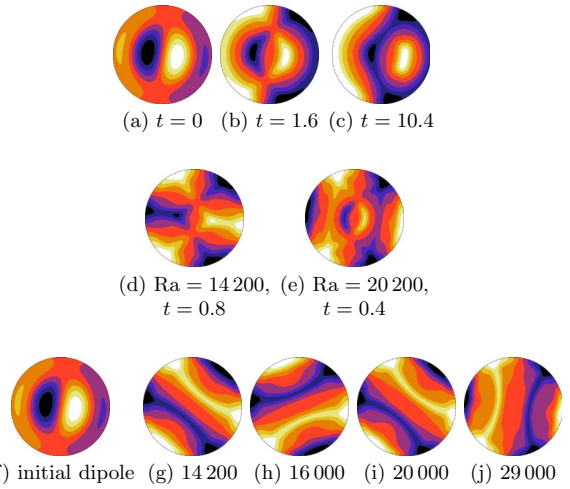

FIG. 10. (Color online) Evolution from dipole pattern. (a)–(c) Through dipole smile into final CO pattern at Ra=10 000. (d)–(e) Transitional patterns observed during evolution from dipole into three-roll pattern. (f) Initial dipole and (g)–(j) final patterns at Rayleigh numbers indicated.

10. Dipole-shaped perturbation

As in Sec. III A 2, we again used as an initial condition a low-amplitude state. This initial condition was obtained as follows. We began with the three-roll state converged at Ra =14 200 and lowered Ra to 1200, i.e., below the convective threshold. A transient dipole appeared, similar to that depicted in Fig. 4(c), and we halted the evolution before the flow reverted to the conductive state. Although this initial condition is not a converged pattern, it occurs during the evolution of the system and is thus reachable experimentally.

Starting with this initial condition, simulation yields a dipole at Ra=2000 and three rolls at Ra=5000. However, for $10\,000 \leq \mathrm{Ra} \leq 15\,000$, we obtain a different and unusual state. A transitional dipole smile gives way to a slowly rotating roll in the shape of the letter S, which we will refer to

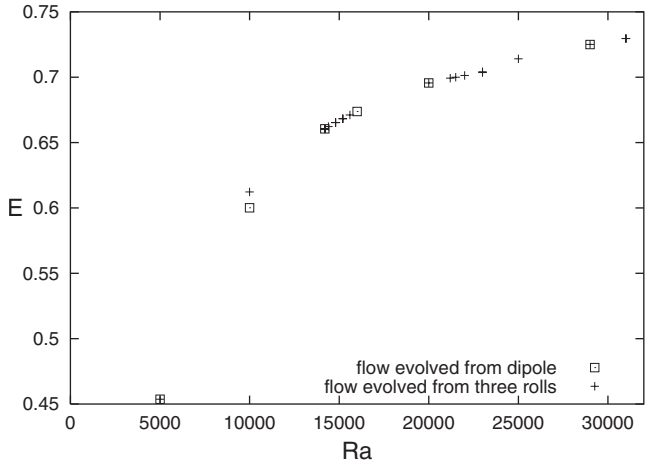

FIG. 11. Squares, energy of the flow evolved from dipole state as a function of Rayleigh number; crosses, energy of the flow evolved from three-roll state (for comparison). At Ra=10 000 the dipole pattern evolved into a CO pattern.

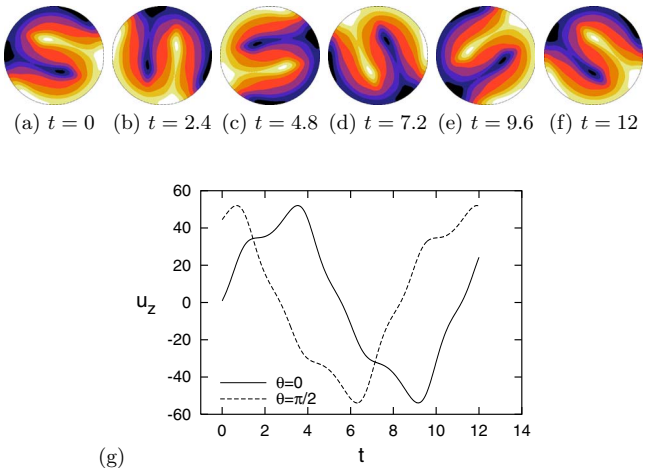

FIG. 12. (Color online) Rotating S pattern at Ra=12 500. (a)–(f) Visualizations at six different times. (g) Evolution in time of vertical velocity at two points with the same r and z and different θ.

as a *rotating S* pattern. This time-dependent state resembles a truncated version of the rotating spiral found in simulations in a $\Gamma=4$ geometry [19]. A visualization of the rotating S at different times is displayed in Figs. 12(a)–12(f) and the evolution of the temperature at two points is plotted in Fig. 12(g). The rotation is very slow: one period is on the order of 10, and the frequency grows with the Rayleigh number. Figure 13 shows the dependence of the frequency and energy of the rotating S on Rayleigh number.

The evolution of the dipole pattern at Ra=16 000 is shown in Fig. 14. It passes through an intermediate *three-part dipole pattern* before finally becoming a dipole-smile pattern. This pattern, observed for $5000 \leq \mathrm{Ra} \leq 15\,000$ as

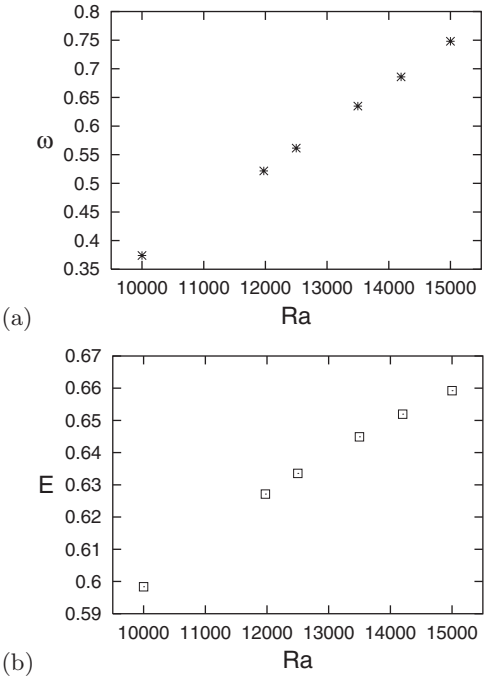

FIG. 13. (a) Frequency and (b) energy of the rotating S pattern as a function of Rayleigh number.

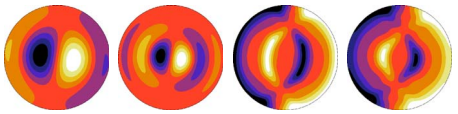

(a) $t=0$ (b) $t=0.2$ (c) $t=0.6$ (d) $t=1.2$

FIG. 14. (Color online) Evolution from dipole-shaped perturbation into a stable smile pattern at Ra=16 000.

a transient pattern, seems to be stable for this Rayleigh number.

For 20 000 $\leq$ Ra $\leq$ 29 000, the dipole pattern transforms at first into a transitional pattern, similar to dipole smile, then into an S roll, and finally it becomes a stable three-roll flow. The transition occurs without any oscillatory evolution and the energy of the final state fits the previously observed dependence between three-roll pattern energy and Rayleigh number in Fig. 11.

11. Summary diagrams

The energy of all stable patterns described above, as a function of Rayleigh number, is depicted in Fig. 15(a). The energy depends on the type of convective pattern, as well as on the value of Ra, but the values for different patterns obtained at the same Ra are very close.

Figure 15(b) shows a preliminary bifurcation diagram. We define $\bar{H}$ to be the maximum absolute value of the temperature deviation over the ring at $(r=0.3, \theta, z=0)$,

$$\bar{H} \equiv \max_{\theta} |H(r=0.3, \theta, z=0)|. \tag{12}$$

$\bar{H}$ itself (as well as the commonly used Nusselt number) has a strong linear dependence on Ra; plotting them directly as a function of Ra does little to separate the branches and this is why we have chosen to represent each state by its value of $\bar{H}/\mathrm{Ra}$.

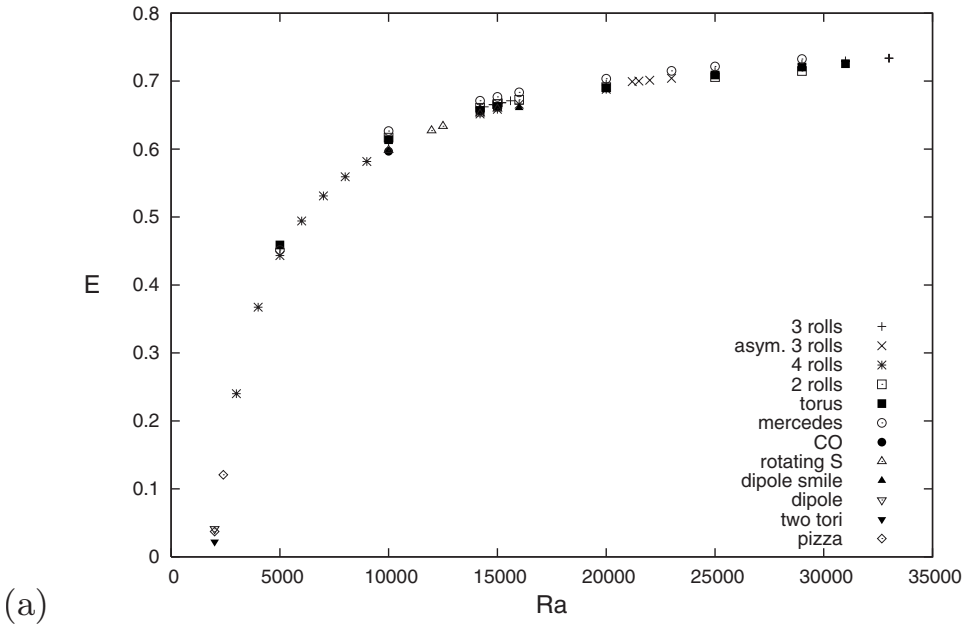

(a)

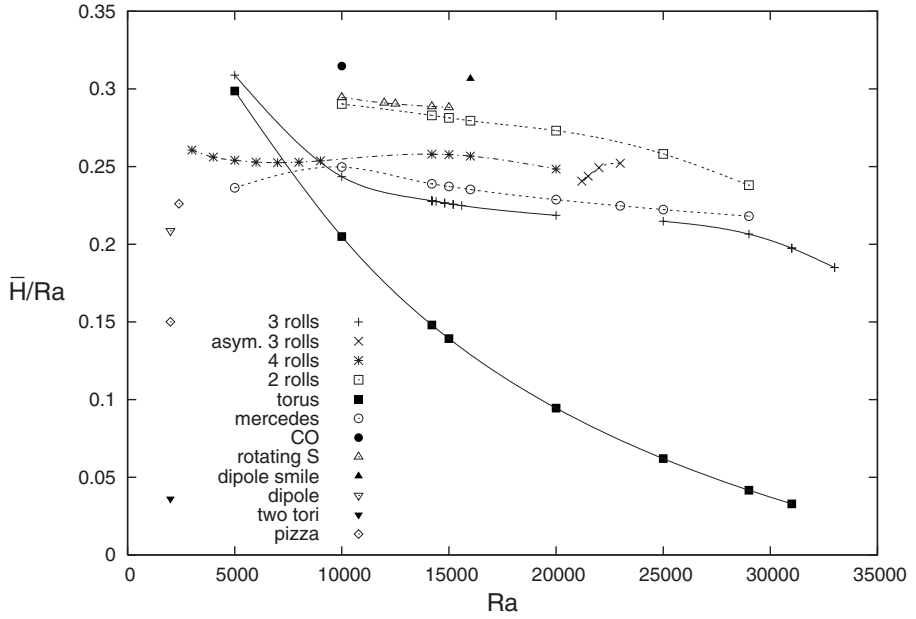

(b)

FIG. 15. Dependence on Rayleigh number of (a) energy and (b) scaled temperature deviation $\bar{H}/\mathrm{Ra}$ for all stable convective patterns obtained for insulating sidewalls.

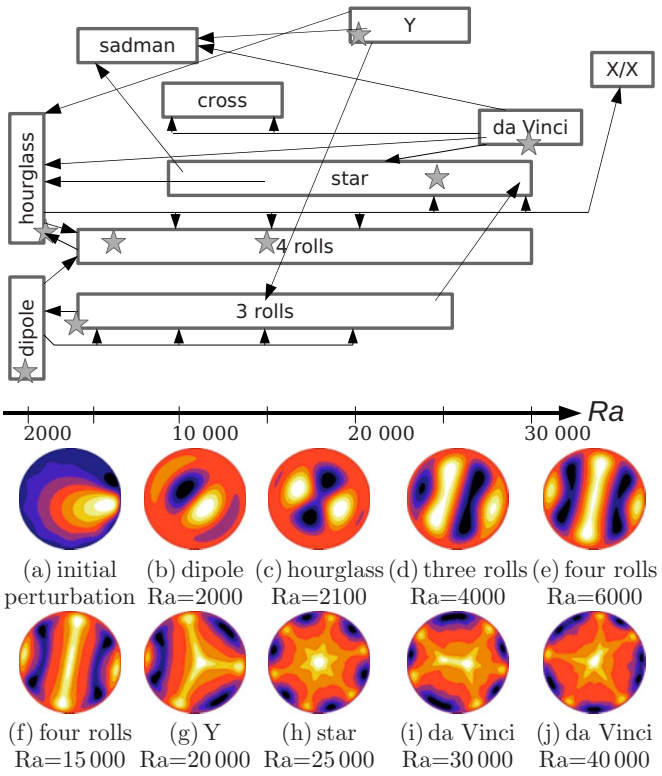

FIG. 16. (Color online) Schematic diagram of stability ranges and transitions between convective patterns as a function of Rayleigh number for $\Gamma=2$, Pr=6.7 and conducting sidewalls. Stars denote solutions obtained from a slight perturbation of the conductive state, at given Ra. (a) Arbitrary perturbation used for initializing simulations and (b)–(j) final patterns at various Rayleigh numbers.

B. Conducting sidewalls

We now present results obtained for perfectly conducting sidewalls, i.e., we apply homogeneous Dirichlet boundary conditions (3d) instead of Neumann boundary conditions (3c). The configuration is otherwise identical, i.e., $\Gamma=2$ and Pr=6.7. A schematic diagram organizing all the results we will present is shown in Fig. 16.

1. Sudden start from perturbed conductive state

As before, we initialized the first series of simulations with a perturbed conductive solution at various Rayleigh numbers between 1900 and 40 000. The initial perturbation and final states are displayed in Figs. 16(a)–16(j) . For Ra =1900 and 2000 the final state is of dipole form. For $2100 \leq \mathrm{Ra} \leq 2500$, instead of the pizza pattern observed for the insulating case, we found an *hourglass* pattern, with elongated cold spots touching at the center. For Ra=2700 and 4000 we obtained three rolls and for $6000 \leq \mathrm{Ra} \leq 15\,000$ four rolls, which differ from the analogous patterns described previously only at the sidewalls, since, here, the deviation from the conductive profile must be zero at the boundaries. For Ra=20 000 we observed a *Y pattern*, shown in Fig. 16(g), with three bands of hot fluid in the shape of the letter Y. It is similar to the previously observed Mercedes pattern, but has only one and not three symmetry axes. For Ra =25 000 we obtained a state in the form of a six-armed star,

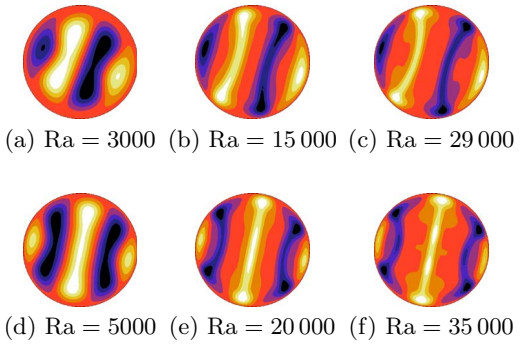

FIG. 17. (Color online) Roll patterns at different Rayleigh numbers. (a)-(c) Three-roll patterns. (d)-(f) Four-roll patterns.

presented in Fig. 16(h). For Ra=30 000 and above, up to 40 000, we obtained a pattern we call *da Vinci*, because of its resemblance with the artist's sketch of human body proportions as shown in Figs. 16(i) and 16(j). All of these flows were stationary.

2. Three rolls

In this series of simulations we used as the initial condition the three-roll pattern in Fig. 16(d). We then obtained stable three-roll patterns for wide ranges of Rayleigh numbers $3000 \leq \mathrm{Ra} \leq 24\,000$ and $26\,000 \leq \mathrm{Ra} \leq 29\,000$, as shown in Figs. 17(a)–17(c). At Ra=25 000 the flow seems to evolve instead toward a two-roll state. (We can, however, obtain a three-roll pattern at Ra=25 000 by initializing the simulation with three rolls obtained at Ra=20 000.) For Ra =30 000, the simulation evolves to a star pattern.

3. Four rolls

Every four-roll pattern we used as initial condition retained its structure within a large range of Rayleigh numbers $5000 \leq \mathrm{Ra} \leq 35\,000$, as shown in Figs. 17(d)–17(f). For Ra =2000 the initial four-roll flow evolves into an hourglass pattern like that in Fig. 16(c) and at Ra=40 000 it remains a four-roll pattern, but with the roll boundaries vibrating slightly with an oscillation period $T=0.026$.

4. Evolution from dipole pattern

When we used the dipole pattern in Fig. 16(b) as an initial condition at higher Rayleigh numbers, the flow evolved into three rolls for Ra=5000 and four rolls for $10\,000 \leq \mathrm{Ra} \leq 20\,000$. For Ra=25 000 we obtained a Y pattern like that in Fig. 16(g). For Ra=30 000 the simulation evolves initially toward a three-roll state, and so eventually should reach a star pattern, as ascertained in Sec. III B 2.

5. Evolution from hourglass pattern

For simulations initialized with the hourglass pattern shown in Fig. 16(c) we obtained a stable hourglass pattern for Ra=2000, four-roll flow for $5000 \leq \mathrm{Ra} \leq 20\,000$, and a six-armed star for Ra=25 000 and 30 000. For $\mathrm{Ra} \geq 35\,000$ a new standing-wave pattern appears. This state oscillates between left- and right-tilted X-letter shapes, passing via inter-

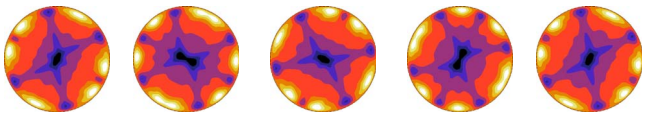

(a) $t=0$ (b) $t=0.25T$ (c) $t=0.5T$ (d) $t=0.75T$ (e) $t=T$

FIG. 18. (Color online) Oscillatory X/X pattern at Ra=35 000.

mediate starlike patterns; see Fig. 18. The oscillation period of this X/X state is $T=3.05$.

6. Evolution from star pattern

In order to obtain patterns in the form of a six-armed star, we used as initial condition the star flow converged at Ra =25 000. Several final convective structures obtained for different Rayleigh numbers are presented in Fig. 19. The star flow remains stable for $10\,000 \leq \mathrm{Ra} \leq 30\,000$, shown in Figs. 19(a) and 19(b)]. Below this range the initial pattern evolved into a *sadman pattern*, as in Fig. 19(c) at Ra=5000 and an hourglass pattern at Ra=2000. For both Ra=2000 and 5000, axisymmetric transient patterns appear. For Ra=2000 the transient state is composed of two concentric toroidal rolls, and its lifetime is about 30. Figure 19(e) shows the evolution of the energy during the transition from the initial star flow, through a long-lasting axisymmetric state into the asymptotic hourglass pattern. While the flow is axisymmetric, the energy remains almost constant.

7. Evolution from da Vinci pattern

The da Vinci pattern shown in Fig. 16(i)], used as initial condition, was stable only for $\mathrm{Ra} \geq 30\,000$. For lower Rayleigh numbers the simulation evolves toward hourglass at 2000, sadman at 5000, a cross at 14 200 and 10 000, shown

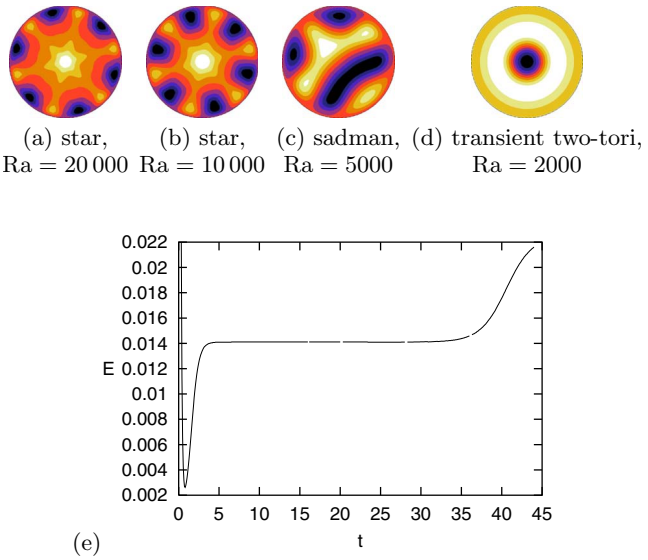

(a) star, Ra = 20 000 (b) star, Ra = 10 000 (c) sadman, Ra = 5000 (d) transient two-tori, Ra = 2000

(e)

FIG. 19. (Color online) (a)–(d) Convective patterns evolved from star flow. (e) Evolution of the system initialized with star pattern at Ra=2000: energy as a function of time. Between $t=5$ and 35 there is a long-lasting transient axisymmetric pattern.

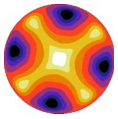

FIG. 20. (Color online) Cross pattern evolved at Ra=10 000 from da Vinci flow.

in Fig. 20, and a stable five-armed star at 20 000 and seemingly also at 25 000.

8. Evolution from Y pattern

Having obtained the Y pattern at Ra=20 000 we reused it as an initial condition. We found stable Y flows for Rayleigh numbers $20\,000 \leq \mathrm{Ra} \leq 25\,000$. For Ra=14 200 the evolution led to three rolls. For lower Rayleigh numbers we obtained sadman patterns at Ra=10 000 and 5000 and hourglass at Ra=2000. Since there is a resemblance between the sadman and Y patterns, these may be related.

9. Summary diagrams

Figure 21(a) shows the energy of all stable patterns found for Dirichlet thermal boundary condition. As in the case of insulating sidewalls, the energy depends primarily on Rayleigh number, with a slight variation between types of convective patterns. Figure 21(b) shows $\bar{H}/\mathrm{Ra}$, as defined in Eq. (12), plotted as a function of Rayleigh number, for all stable patterns found. For higher Rayleigh numbers, several patterns remain stable over large intervals of Ra: three rolls, four rolls, and star. Patterns da Vinci, Y, and cross were observed in smaller ranges. For lower Rayleigh numbers we observed only two stable patterns: dipole and hourglass.

IV. CONCLUSION

We have performed simulations with aspect ratio $\Gamma=2$ and Prandtl number Pr=6.7, matching the configuration of Hof *et al.* [1], who observed experimentally several different convective patterns at the same Rayleigh number. While their sidewalls were well insulating, we ran the simulations for both perfectly conducting and perfectly insulating sidewalls. The results of our simulations for insulating sidewalls are in good agreement with the experiment: we succeeded in obtaining all five steady patterns observed experimentally for Ra=14 200. For the same Rayleigh number we observed the five stable steady solutions they reported: a toroidal roll; two, three, and four parallel rolls; and a three-spoke (Mercedes) pattern. Additionally, we obtained an unusual rotating S structure.

For both types of boundary conditions we found multiple stable solutions for the same Rayleigh number. We preserved the nomenclature of Hof [2] and gave names to patterns not previously reported. We presented summary diagrams organizing the complicated dependencies between the coexisting stable solutions. Our simulations confirm the fact that, even for cylinders of small aspect ratio, the form of the convective flow depends not only on Rayleigh number, but also dramatically on the initial condition. Furthermore, even for Rayleigh

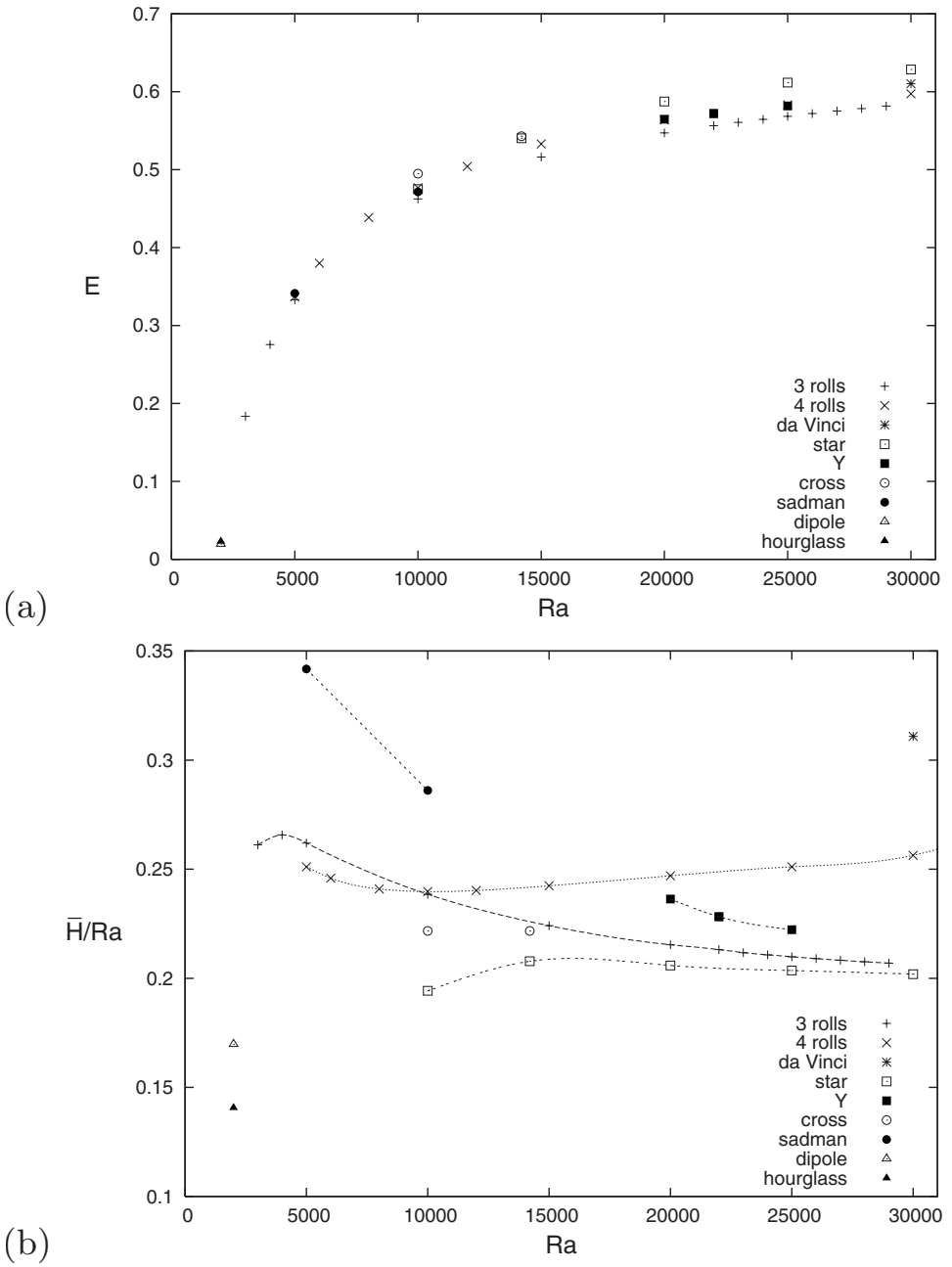

FIG. 21. Dependence of Rayleigh number of (a) energy and (b) scaled temperature deviation $\bar{H}/\mathrm{Ra}$ for all stable convective patterns obtained for conducting sidewalls.

number as low as 2000, we found up to three different long-lived patterns.

The behavior of the system depends both qualitatively and quantitatively on the boundary conditions. For higher Rayleigh numbers and perfectly insulating boundary conditions, among the patterns we obtain are two, three, and four rolls, torus, Mercedes, and dipole smile. When we change the sidewalls to perfectly conducting, only three and four rolls can be observed. The axisymmetric state disappears and the Mercedes state is replaced with the Y flow, thus losing its threefold reflection symmetry. On the other hand, for conductive sidewalls, new cross, da Vinci, and star flows appear. The other patterns, such as two rolls or dipole smile, may or may not also exist for conducting sidewalls. At lower Rayleigh numbers, insulating boundaries yield dipole, pizza, and axisymmetric patterns. For conducting boundaries the dipole flow also exists, but the pizza pattern is replaced with hourglass and an axisymmetric pattern appears only as a transient state. In general, it seems that switching to perfectly conducting sidewalls makes some of the patterns lose their symmetries. This transition could be elucidated by performing a study in which intermediate values of sidewall conductivity would be used, and checking how the flow symmetry changes.

Close to the threshold (at Ra=2000), for both types of boundary conditions, we observed different stable patterns, but none of them seem to be stable at higher Rayleigh number; conversely none of the patterns observed at higher Ra could be observed at Ra=2000. In a companion paper [24], we use Newton's method to construct a bifurcation diagram relating the states found at low Ra to those found at high Ra, for the case of insulating sidewalls. In contrast to time step-

ping, Newton's method converges more rapidly and regardless of stability. The time-stepping procedure we used here lets us follow the dynamics known from the experimental scenario, including transitions between the steady and time-dependent states. The patterns we obtained have constituted a good preliminary survey for constructing a complete bifurcation diagram via continuation. This task has not yet been undertaken for the case of conducting sidewalls.

It is very likely that other stable solutions exist, which we did not observe because they were topologically too far from any of our initial conditions. We observed several time-dependent flows not reported by Hof *et al.* [1], but we believe that we are far from describing all existing unsteady solutions in the range of Rayleigh numbers simulated. Except for the rotating S pattern, which exists for $\mathrm{Ra} \approx 15\,000$, we observed oscillations mainly above $\mathrm{Ra}=30\,000$. Hof *et al.* [1] also observed a three-petal rotating pattern at $\mathrm{Ra}=23\,000$ and a 13-spoke pulsing pattern at $\mathrm{Ra}=33\,000$; it would be interesting to reproduce these and to ascertain whether they result from a Hopf bifurcation by a scenario like that described in our previous paper [33]. We showed the existence of several long-lasting transient states, for example, in the case of initialization with a dipole pattern and conducting boundaries, for which the dipole smile state persisted for some time, with relatively constant energy, before transforming into the final three-roll flow. This and other transitional patterns could also be objects for further study. Despite the great variety of flows we have obtained, we are far from an exhaustive study even for this specific configuration of control parameters.

Although small-aspect-ratio cylinders lack the universality of large ones, our three-dimensional numerical study has illustrated the remarkable variety of convective flows and rich dynamics found in this system. We hope that our results convince the reader that this chapter of hydrodynamical research is not yet thoroughly written.

ACKNOWLEDGMENTS

We gratefully acknowledge the contributions of Daniel Benaquista to this work. We thank Tom Mullin and Björn Hof for their continued interest in this work. All of the computations were performed on the computers of Institut pour le Developpement des Ressources Informatiques et Scientifiques (IDRIS) of Centre National pour la Recherche Scientifique (CNRS) under Project No. 1119.

[1] B. Hof, G. J. Lucas, and T. Mullin, Phys. Fluids **11**, 2815 (1999).
[2] B. Hof, Master's thesis, University of Manchester, 1997.
[3] G. Charlson and R. Sani, Int. J. Heat Mass Transfer **13**, 1479 (1970).
[4] G. Charlson and R. Sani, Int. J. Heat Mass Transfer **14**, 2157 (1971).
[5] K. Stork and U. Müller, J. Fluid Mech. **71**, 231 (1975).
[6] J. Buell and I. Catton, J. Heat Transfer **105**, 255 (1983).
[7] E. L. Koschmieder, *Bénard Cells and Taylor Vortices* (Cambridge University Press, Cambridge, England, 1993).
[8] F. Marques, M. Net, J. M. Massaguer, and I. Mercader, Comput. Methods Appl. Mech. Eng. **110**, 157 (1993).
[9] G. Müller, G. Neumann, and W. Weber, J. Cryst. Growth **70**, 78 (1984).
[10] G. Hardin and R. Sani, Int. J. Numer. Methods Fluids **17**, 755 (1993).
[11] M. Wanschura, H. C. Kuhlmann, and H. J. Rath, J. Fluid Mech. **326**, 399 (1996).
[12] R. Touihri, H. Ben Hadid, and D. Henry, Phys. Fluids **11**, 2078 (1999).
[13] D. Barkley and L. S. Tuckerman, Physica D **37**, 288 (1989).
[14] J. H. Siggers, J. Fluid Mech. **475**, 357 (2003).
[15] A. Pocheau, V. Croquette, and P. Le Gal, Phys. Rev. Lett. **55**, 1094 (1985).
[16] V. Croquette, Contemp. Phys. **30**, 113 (1989); **30**, 153 (1989).
[17] V. Steinberg, G. Ahlers, and D. S. Cannell, Phys. Scr. **32**, 534 (1985).
[18] F. Busse and R. Clever, J. Fluid Mech. **91**, 319 (1979).
[19] S. Rüdiger and F. Feudel, Phys. Rev. E **62**, 4927 (2000).
[20] M. R. Paul, K. H. Chiam, M. C. Cross, P. F. Fischer, and H. S. Greenside, Physica D **184**, 114 (2003).
[21] S. S. Leong, Numer. Heat Transfer, Part A **41**, 673 (2002).
[22] D.-J. Ma, D.-J. Sun, and X.-Y. Yin, Phys. Rev. E **74**, 037302 (2006).
[23] K. Borońska, Ph.D. thesis, Université de Paris 7, 2005.
[24] K. Borońska and L. S. Tuckerman, following paper, Phys. Rev. E **81**, 036321 (2010).
[25] L. S. Tuckerman, J. Comput. Phys. **80**, 403 (1989).
[26] D. Gottlieb and S. A. Orszag, *Numerical Analysis of Spectral Methods: Theory and Applications* (SIAM, Philadelphia, 1977).
[27] C. Temperton, J. Comput. Phys. **75**, 199 (1988).
[28] C. Canuto, M. Y. Hussaini, A. Quarteroni, and T. A. Zang, *Spectral Methods in Fluid Dynamics* (Springer-Verlag, Berlin, 1988).
[29] L. S. Tuckerman, J. Comput. Phys. **84**, 360 (1989).
[30] D. Rempfer, Appl. Mech. Rev. **59**, 107 (2006).
[31] C. Rappaport, IEEE Antennas Propag. Mag. **44**, 94 (2002).
[32] B. Hof (private communication).
[33] K. Borońska and L. S. Tuckerman, J. Fluid Mech. **559**, 279 (2006).